

Quarterly Report for
Contract DE-FG36-08GO18192
Stanford Geothermal Program
January-March 2009

Table of Contents

1. FRACTURE CHARACTERIZATION USING PRODUCTION AND INJECTION DATA	1
1.1 SUMMARY	1
1.2 NONPARAMETRIC REGRESSION MODELS APPLIED TO PRODUCTION AND INJECTION DATA	1
1.3 DISCRETE FRACTURE NETWORK MODELING	9
1.4 FUTURE WORK	15
1.5 CONCLUSIONS	15
2. FRACTURE CHARACTERIZATION OF ENHANCED GEOTHERMAL SYSTEMS USING NANOPARTICLES	17
2.1 SUMMARY	17
2.2 INTRODUCTION	17
2.3 REQUIREMENTS FOR NANOPARTICLES	17
2.4 EXPERIMENTS	20
2.5 FUTURE WORK	28
3. REFERENCES	29

1. FRACTURE CHARACTERIZATION USING PRODUCTION AND INJECTION DATA

This research project is being conducted by Research Assistant Egill Juliusson, Senior Research Engineer Kewen Li and Professor Roland Horne. The objective of this project is to investigate ways to characterize fractures in geothermal reservoirs using injection and production data.

1.1 SUMMARY

This project involves fracture characterization utilizing nonparametric regression methods to extract information from production and injection data.

Investigation of this methodology is still in the early stages. However, preliminary results indicate that, with an appropriate data set, signals from multiple producers and injectors could be decoupled, thereby providing important information about the structure of the subsurface flow paths. These results have been verified using simplified synthetic data sets.

Currently effort is being put into generating more realistic data sets, which can be used for further experimentation with various types of inversion methods. This involves running flow simulations on unstructured grids with fractures treated as discrete objects.

1.2 NONPARAMETRIC REGRESSION MODELS APPLIED TO PRODUCTION AND INJECTION DATA

Nonparametric regression models have been used in a few recent studies to infer the connection between measured values in injection and production wells (e.g. Fienen et al., 2006; Horne and Szucs, 2007; Nomura and Horne, 2009). The advantage of using such models is that they allow a suitable level of information extraction while imposing only minimal constraints on the underlying relationship between the input data and the underlying reservoir model. This way, indirect information on the subsurface structure of the reservoir could be revealed using standard production data, such as pressure, temperature, enthalpy or chemical concentration fluctuations with time.

1.2.1 Alternating Conditional Expectation (ACE) method applied to synthetic tracer return data

As an initial step towards understanding the capabilities of nonparametric methods we applied the Alternating Conditional Expectation (ACE) algorithm developed by Breiman and Friedman in 1985 on some synthetic tracer return data. The ACE algorithm is a nonparametric method that can be used to infer the “most likely” relationship between multiple predictor data sets and a single response data set. The only prior assumption is that the transfer function between the two has a certain degree of smoothness.

Given a response signal, y , and multiple predictors, x_i , the ACE algorithm will find the transformations Θ and Φ_i that give the maximum possible correlation between $\Theta(y)$ and the sum of $\Phi_i(x_i)$, subject to the constraint that the transformed data must retain a certain level

of continuity (or smoothness). That is, it finds the optimum transformations Θ and Φ_i that fulfill the equation:

$$\Theta(y) = \sum_i^{Np} \Phi_i(x_i) \quad (1.1)$$

subject to a smoothness constraint. More details on the algorithm can be found in the reference by Breiman and Friedman (1985).

Our idea was to investigate the applicability of using ACE to reveal the relationship between tracer injection into multiple wells and the tracer produced in a single production well. To start the investigation, synthetic data were generated, describing the return of tracer for continuous injection of material with concentration C_o into a one-dimensional column:

$$C = \frac{C_o(t)}{2} \operatorname{erfc} \left[\frac{d - ut}{2\sqrt{\eta t}} \right] + e \quad [-] \quad (1.2)$$

Here C is the concentration of tracer return, $C_o(t)$ is the concentration of tracer injected at time t , erfc is the complimentary error function, d is the distance between the producer and injector, u is the average travel velocity (Darcy velocity) of the tracer, η is the dispersivity [m^2/s] of the medium and e is Gaussian error that was added to the data. Some example return curves are shown in Figure 1.1 (here $e = 0$).

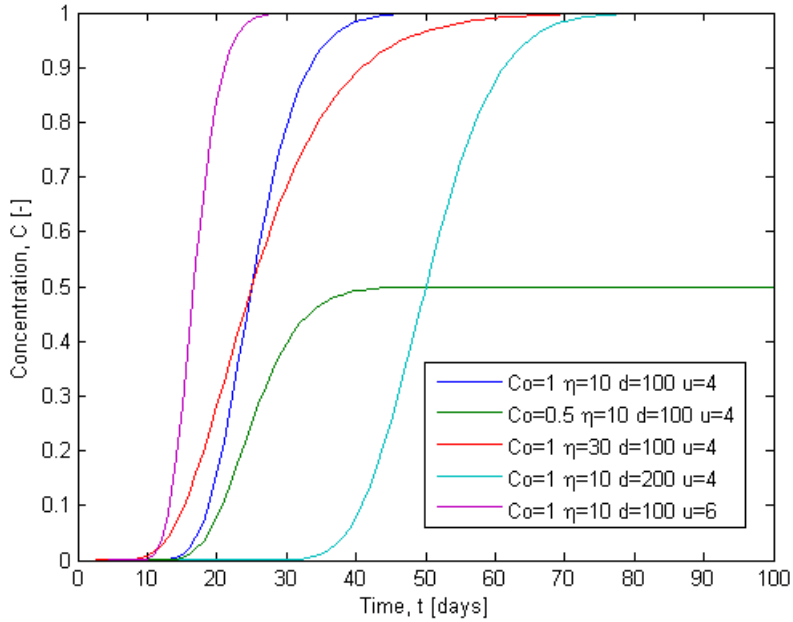


Figure 1.1: Illustrates how some simple synthetic tracer return curves vary with the model parameters. These are the response to a C_o step injection of tracer at time $t=0$.

The ACE algorithm was run with a C_o increase in injection at time $t = 10$ as a predictor data set, $x(t)$, and the blue curve in Figure 1.1 as the response, $y(t)$. The ACE algorithm then found the transformations, $\Theta(x)$ and $\Phi(y)$, which make the two variables as close as possible. Figure 1.2 shows the input data and Figure 1.3 shows the transformations of the data.

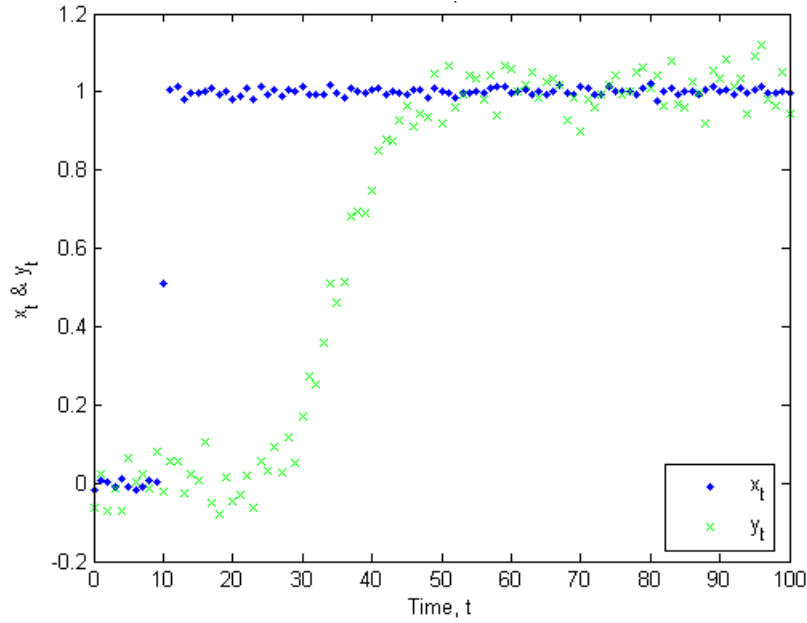


Figure 1.2: The curves used in a simple data set used to test the applicability of using the ACE algorithm to recover the transformation between a predictor and a response.

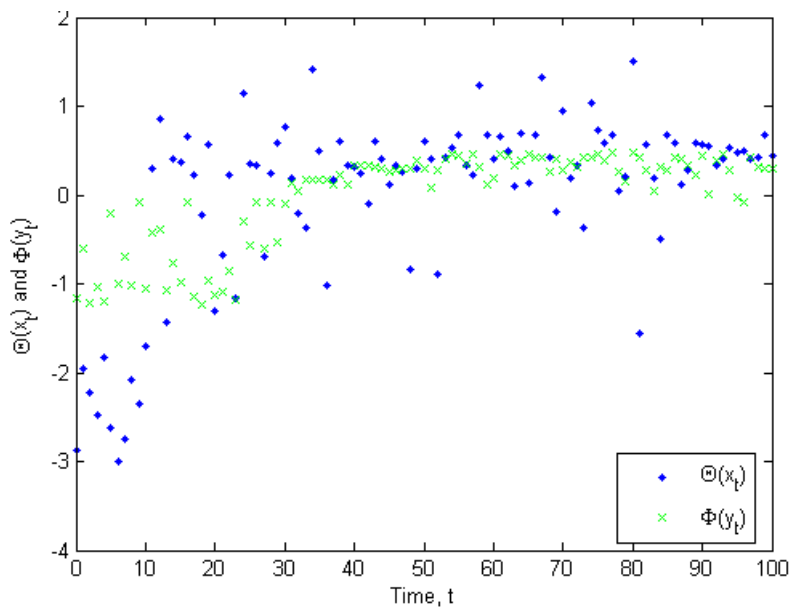


Figure 1.3: The resulting transformations of the predictor and response shown in Figure 1.2. The algorithm does a poor job of predicting the optimal transformation which can be seen from the relatively low correlation coefficient $R^2=0.59$.

These figures indicate the algorithm does a rather poor job of recovering the transformation between x and y . This is confirmed by the relatively low correlation coefficient $R^2=0.59$.

In an effort to improve the performance of the algorithm we tried to shift the response function in time, such that it would take on a form more similar to the predictor. This improved the correlation coefficient considerably, bringing it up to about 0.85 with the correct time shift. Testing several other simple cases revealed that the correlation coefficient reached a maximum value close to the actual travel time, $t_{actual} = u/d$, of the tracer.

Being able to predict the travel time from simple signals like the ones shown in Figure 1.2 is a trivial matter; however that task becomes more complicated given the response to multiple predictors. For example we could consider the effects that reinjecting brine with high chemical concentration into multiple injection wells would have on the chemicals recovered in a producer. In actual geothermal fields the reinjection into each well takes place at variable rates and the concentration of the injected brine will also vary with time. So all of the coefficients, $C_o(t)$, u , d , and η in Equation 1.1 will vary depending on the location of the injector and the time at which each injector is turned on and off. Figure 1.4 shows a synthetic scenario where three injectors are turned on and off at various times and the amount of injected chemical concentration varies from time to time. The response was generated based on Equation 1.1 with randomized values of $C_o(t)$, u , d , and η . Note that the concentration of chemicals is a direct addition of the individual injected amounts since we are using a one-dimensional approximation to create the response function.

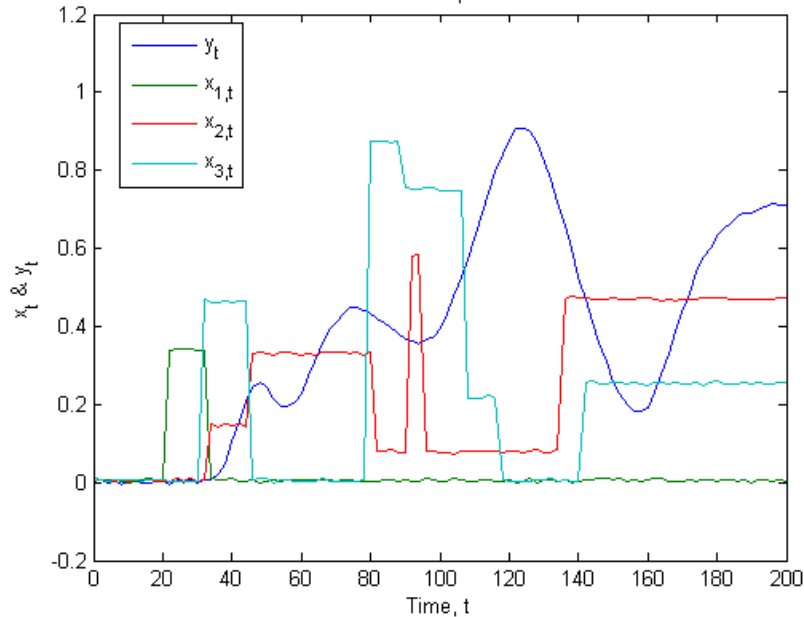


Figure 1.4: A synthetic example of injection (predictors, x) into three wells and the corresponding concentration of chemicals coming out at the producer (response, y).

Figure 1.4 clearly illustrates that predicting the travel time of the chemicals from each injector to the producer is requires more than just “eye-balling” the data. To estimate the individual travel times we systematically shifted each predictor (injector) data set. To cover all possibilities each predictor curve was shifted at reasonable increments dt , up to a

reasonable maximum value t_{max} . This has to be done for all the predictors, N_p . The overall number of possibilities to be tested will be

$$N_{tot} = \left(\frac{t_{max}}{dt} + 1 \right)^{N_p} \quad (1.2)$$

We applied the ACE algorithm to find the optimal transformation between the response and the ensemble of the predictor curves. This was done for all possible time shifts in increments of 2 days over a 40 day range. This amounted to $21^3 \approx 10,000$ possibilities which took about 10 hours to test running a MATLAB code on a 2.66 GHz desktop with 2 GB RAM.

The combination of time shifts that gave the highest correlation between the predictors and response was compared to the actual travel time used to generate the synthetic data. The results were commonly close to the correct values, although the method did fail in quite a few cases. The method could generally not reproduce the exact time shift values since the actual travel times were positive real values, but the search space for the optimal value of the travel time was limited to increments of dt (typically dt was 1 to 4 days). An example solution is shown in Figure 1.5 and Table 1.1 shows the time shift values determined by ACE. Since this approach for determining the travel time of the chemical tracers seemed unreliable and is rather computationally intensive, an alternate method was sought.

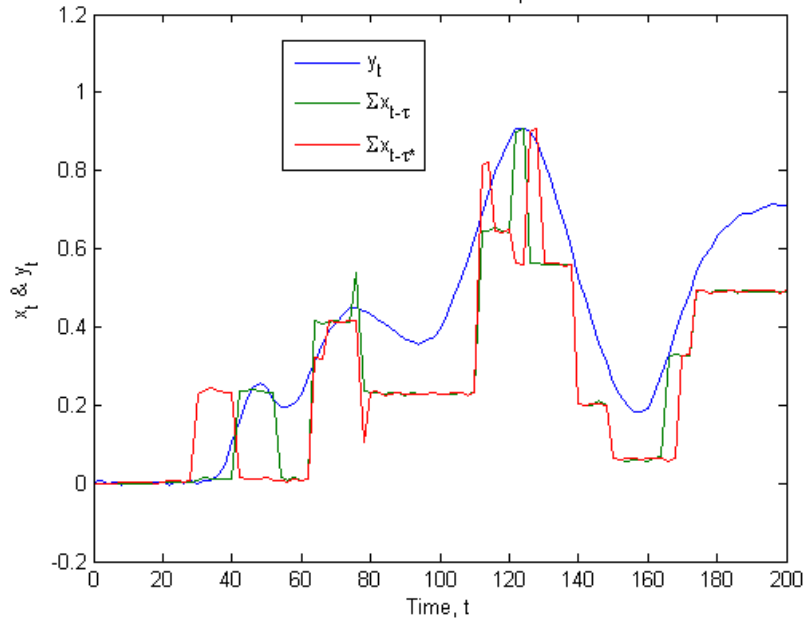


Figure 1.5: This figure shows the response curve shown in Figure 1.4 along with the sum of the time shifted predictor curves as determined by the ACE algorithm, τ^* . The sum of the predictor curves using the actual time shift values, τ , is also shown.

Table 1.1: Time shifts (i.e. travel times) determined by correlating ACE transforms to the response curve, compared with the actual time shifts used to generated the response data.

	τ_1	τ_2	τ_3
Actual (τ)	20.77	30.96	32.59
Predicted (τ^*)	8	34	32

1.2.2 Direct Correlation of sums applied to synthetic tracer return data

As a comparison to the performance of the ACE algorithm in finding the travel times, we set up a similar case using direct correlation between the sum of the time shifted predictor curves (without any previous transformation) and the response curve. This computation ran about 5,000 times faster than using the ACE algorithm. Moreover, this method generally did better than the ACE method in finding the travel times. Figure 1.6 shows the performance of the Direct Correlation method for the data set illustrated in Figure 1.4. The predicted time shifts are presented in Table 1.2. These results are quite typical in illustrating the difference in performance by the two methods.

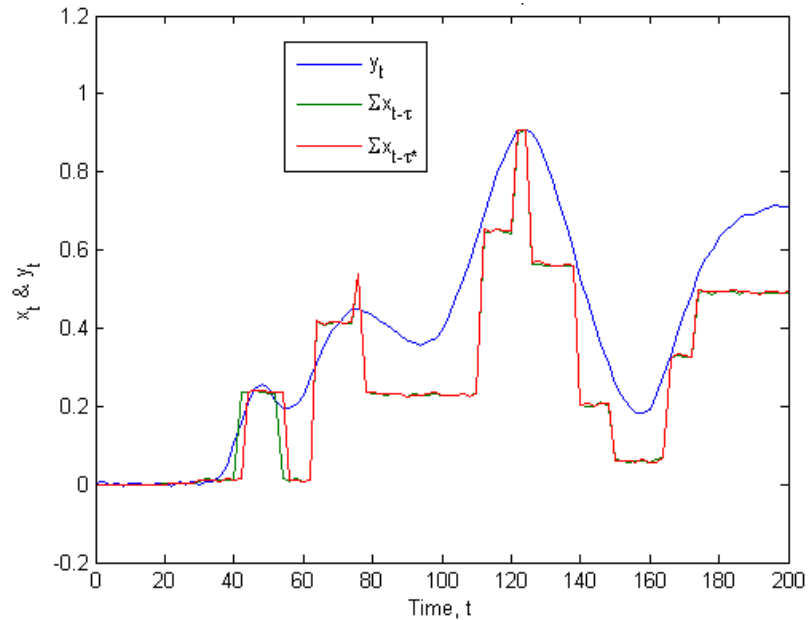


Figure 1.6: This figure shows the response curve shown in Figure 1.4 along with the sum of the time shifted predictor curves as determined by Direct Correlation, τ^* . The sum of the predictor curves using the actual time shift values, τ , is also shown.

Table 1.2: Time shifts (i.e. travel times) determined by Direct Correlation of the sum of three time shifted predictor curves to a response curve, compared with the actual time shifts used to generated the response data.

	τ_1	τ_2	τ_3
Actual (τ)	20.77	30.96	32.59
Predicted (τ^*)	22	30	32

To take the Direct Correlation method a bit further, we tried running it with six producers and a time increment of 1 day for up to 40 days. Since this involved a large amount of trials ($41^6 \approx 5$ billion) we reprogrammed the trial routine in C++. This yielded a 25-fold increase in computation speed, but the run still took about 6 hours. The predictors and response are shown in Figure 1.7. The transfer function from injector to producer is given by Equation 1.1. The input parameters u , d , and η , which are shown in Table 1.3, were randomly selected within reasonable limits.

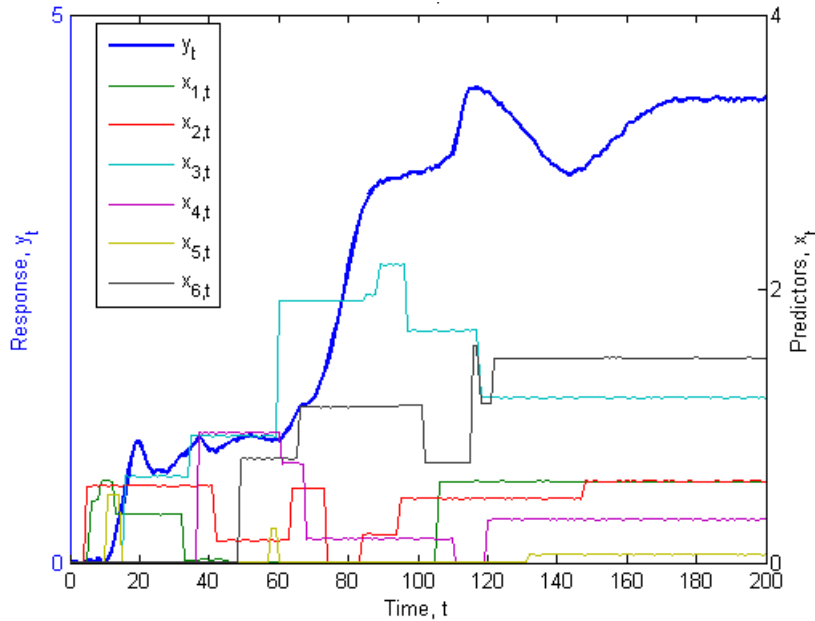


Figure 1.7: This figure shows the synthetic response in chemical concentration of a producer which is connected (in one dimension) to 6 injectors with injection histories as shown in the figure.

The results from this test match surprisingly well as can be seen in Table 1.4 and Figure 1.8. The only travel time that was very far off is that for injector 5. On examining its behavior (Figure 1.7) the reason for this is apparent – the input of injector 5 is very small and therefore contributes very little to the response.

Table 1.3: Parameters used in Equation 1.1 to generate the response curve shown in Figure 1.7.

	Inj. 1	Inj. 2	Inj. 3	Inj. 4	Inj. 5	Inj. 6
u [m/day]	13.77	5.84	3.30	4.58	8.61	4.15
d [m]	95.83	94.65	78.15	160.61	63.33	133.55
η [m ² /day]	28.88	25.04	9.91	24.60	15.31	17.20

Although the Direct Correlation method may have worked quite well in many cases, it did fail regularly, commonly for one or two of the time values. This is highly dependent on the uniqueness and magnitude of the input signal. More gradual changes in the injected concentration would probably degrade the results obtained by both methods, although the ACE method should be less affected. An actual data set that has sufficiently dense concentration measurements and some reference tracer data would of course be ideal to validate the methods further. However, in the absence of such data, we have begun work on generating simulations of flow through discrete fracture networks, as will be described in the next section.

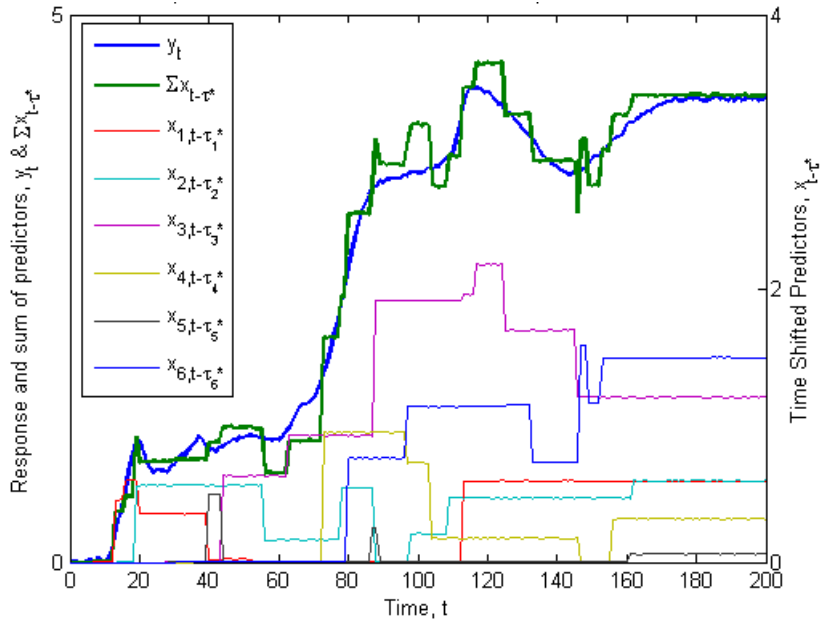


Figure 1.8: Here we show the results of time shifting the predictor curves in such a manner that the sum of the time shifted curves gives the highest correlation to the response. The time shifts correspond to the travel time of the tracer from injector to producer. This Direct Correlation method works surprisingly well, as shown in Table 1.4.

Table 1.4: Time shifts (i.e. travel times) determined by Direct Correlation of the sum of six time shifted predictor curves to a response curve, compared with the actual time shifts used to generated the response data.

	τ_1	τ_2	τ_3	τ_4	τ_5	τ_6
Actual (τ)	6.96	16.22	23.67	35.04	7.36	32.20
Predicted (τ^*)	7	14	28	36	29	31

1.3 DISCRETE FRACTURE NETWORK MODELING

In the past few years, considerable contributions have been made towards creating reservoir simulation models where fractures can be treated discretely as opposed to using course-scale grid blocks with high permeability values. These types of models are of special interest in the geothermal arena since they can more accurately represent the fracture-dominated flow paths generally encountered in geothermal reservoirs.

In 2003, Karimi-Fard et al. published a paper describing a general way of reconfiguring a general reservoir simulator to run with discrete fracture networks. This method can be applied readily to the TOUGH2 reservoir simulator that is commonly used in the geothermal industry, as has been demonstrated by McClure (2008). The reconfiguration process is quite involved and requires generating a set of fractures represented as lines; generating a mesh that conforms to those lines; discretizing the set of fractures and mesh elements in a way such that the description can be run with a general reservoir simulator; setting up and running the reservoir simulator; and finally analyzing the output of the simulation. These last two steps seem trivial but are time consuming since very little effort has been put into improving the usability of TOUGH2.

1.3.1 Synthetic fracture network

Sophisticated algorithms are available for creating geologically realistic synthetic fracture networks in three dimensions, e.g. commercial software packages like FracMan from Golder & Associates and FRACA from Beicip-Franlab. However, for the scope of our work we let it suffice to build an algorithm that generates two-dimensional synthetic fracture networks. The algorithm, which was coded in MATLAB, is loosely based on concepts related to the structural geology of fracture formations. Following is a brief description of how the algorithm works.

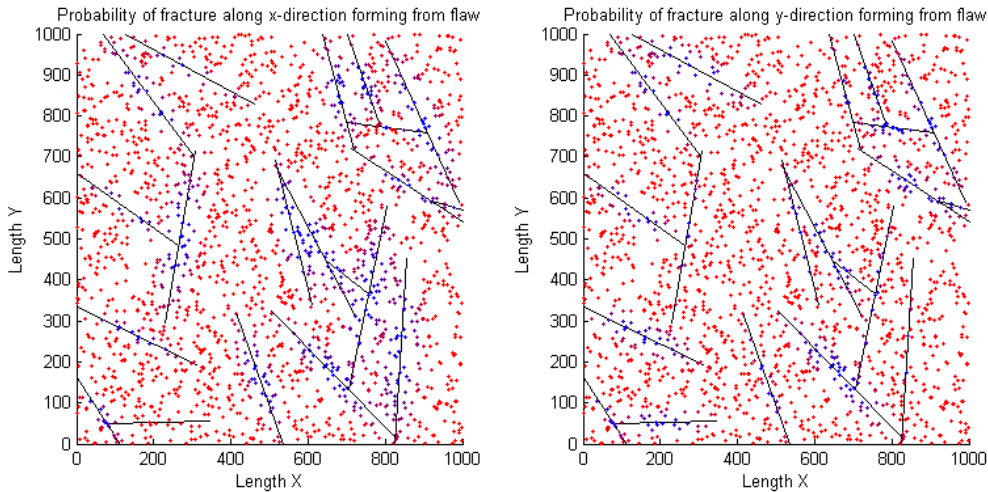


Figure 1.9: An example fracture network with initiation flaws shown as dots in a color spectrum ranging from red to blue. As the color tends to blue there is less probability of a fracture initiating from that flaw.

Initially, a square area is populated with a large number of randomly distributed flaws. Fractures are then generated sequentially, each with an initiation point at one of the flaws. Once a fracture has been created, the probability of a new fracture, with a similar orientation, initiating within a surrounding ellipse is reduced considerably. This effect is meant to be an analogy to the concept of stress relaxation in structural geology. This is illustrated in Figure 1.9. The algorithm has the option of preventing the fractures from propagating through one another. This option is useful since fractures that are open to flow, which are precisely those that we are interested in, tend to terminate the growth of other fractures that form subsequently. Other options include control of the distribution of fracture length, orientation and number of fractures. More options can easily be added; however, with only this limited number of options a remarkable variety of fracture distributions can be created. A few examples are illustrated in Figure 1.10.

1.3.2 Fracture meshing and discretization

The task of generating a mesh that conforms to the fracture boundaries was solved using a mesh-generation software called Triangle, developed by Shewchuk (1996). Each of the elements created by the mesh (i.e. the triangles and fracture segments) must be assigned a transmissibility to enable the use of this mesh with a general reservoir simulator. This procedure is laid out by Karimi-Fard et al. (2003) and will not be described in detail here. Figure 1.11 shows an example of a mesh that conforms to a network of fractures.

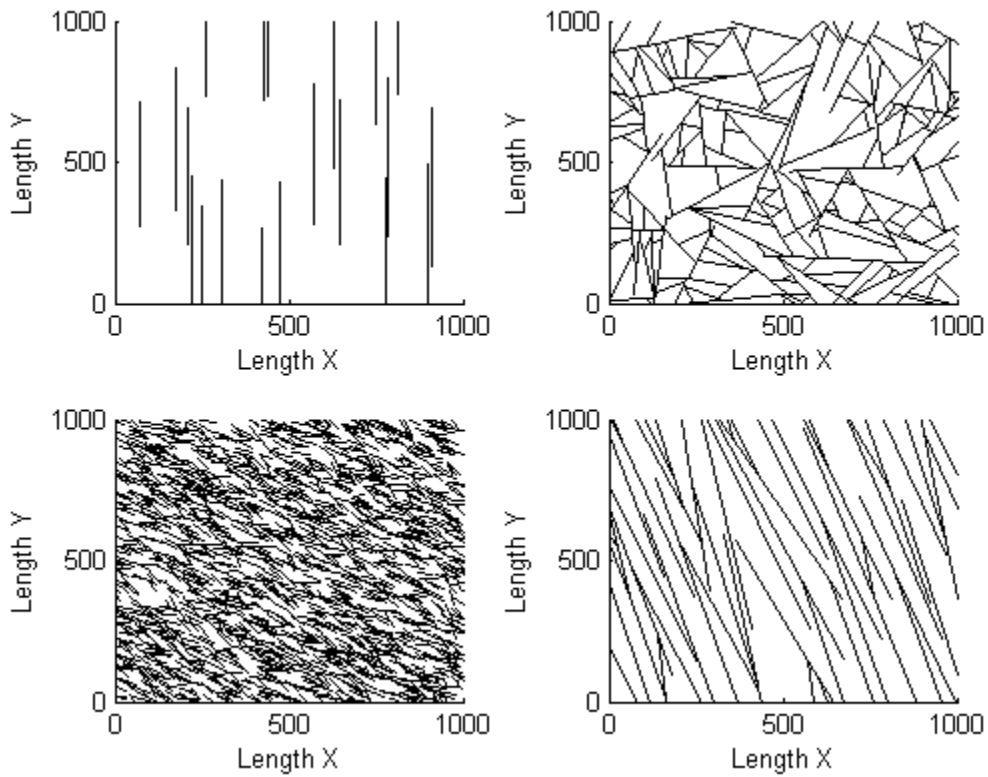


Figure 1.10: As is illustrated in this figure, a remarkable variety of fracture networks can be generated with only a limited number of input parameters, e.g. fracture density, length and orientation.

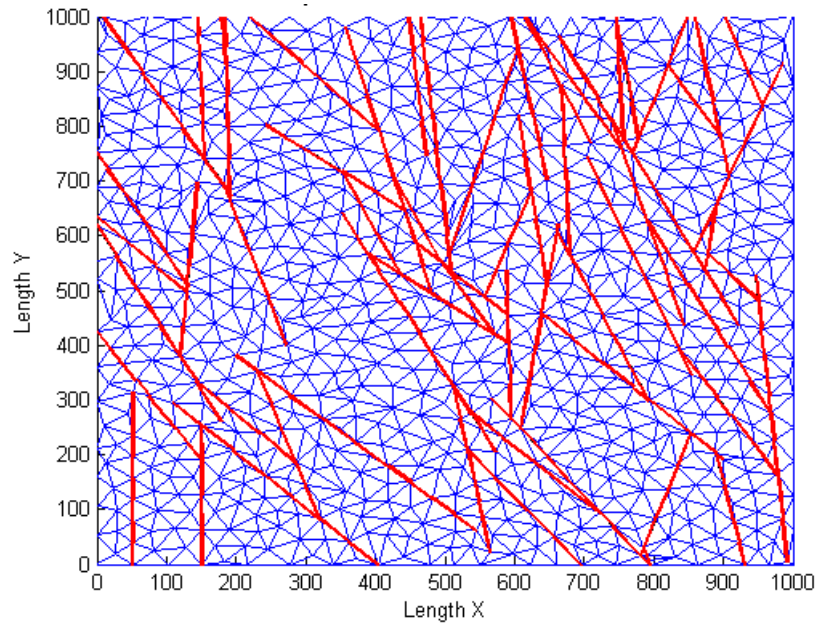


Figure 1.11: A mesh that conforms to the fractures in the fracture network was generated using the mesh generator Triangle, developed by Shewchuk (1996).

1.3.3 Flow simulations

Most recently, some simple flow simulations have been performed, with the discrete fracture networks created, to verify that the method described in the previous section works. So far, only a limited number of subroutines have been written to process the input and output data.

As an interesting case of investigation we ran two simulations of flow through a fracture network. The simulations were identical in all but the reservoir pressure, which was set such that boiling would occur around the production zone in one case, while the other only had single-phase liquid. Both cases considered steady-state flow, with closed boundaries and an initial temperature at 300 °C. The boiling point of water at 300 °C is approximately 85.8 bar. Hence, in first run we set the initial pressure to 86 bar, the injection pressure was fixed at 91 bar and the production pressure was 81 bar, i.e. below the boiling point. In the second run, the initial pressure was 96 bar, injection pressure was fixed at 101 bar and production was at 91 bar. To make sure the temperature in the matrix did not change significantly we set the heat capacity of the rock to a very large number. The permeability and porosity of the matrix were $k_m = 0.1$ md and $\phi_m = 1\%$; the fractures had $k_f = 50,000$ md and porosity $\phi_m = 55\%$. As a precautionary note we must mention that there were some complications with transferring the permeability into TOUGH2. These complications will be studied in more detail at a later date.

The results of the first run, which allowed boiling to occur, are illustrated in Figures 1.12 and 1.13. Figure 1.12 shows the pressure and flow between fracture elements, while Figure 1.13 shows the steam quality and heat transfer between fracture elements. The heat transfer rate from the production element this case was 15 MW and the flow rate was 10.5 kg/s. As can be seen the flow becomes very disperse in between the production and injection zones and the bulk of the produced heat and fluid comes from the fracture/matrix elements around the production zone. This occurs because of expansion of water in the matrix as it boils, which pushes it into the fractures.

The results of the second run are shown in Figures 1.14 and 1.15. In this case the produced heat transfer rate was 5.6 MW and the flow rate was 4.2 kg/s. From a closer look at the figures it is evident that there is more fluid flow in the center between the injection and production zone, which implies that there is a more direct connection between the two (i.e. relative to the first case). Note also that the heat and fluid flow in the fractures immediately surrounding the production zone is smaller, meaning that less fluid is being produced from the matrix than in the case where we let the fluid boil.

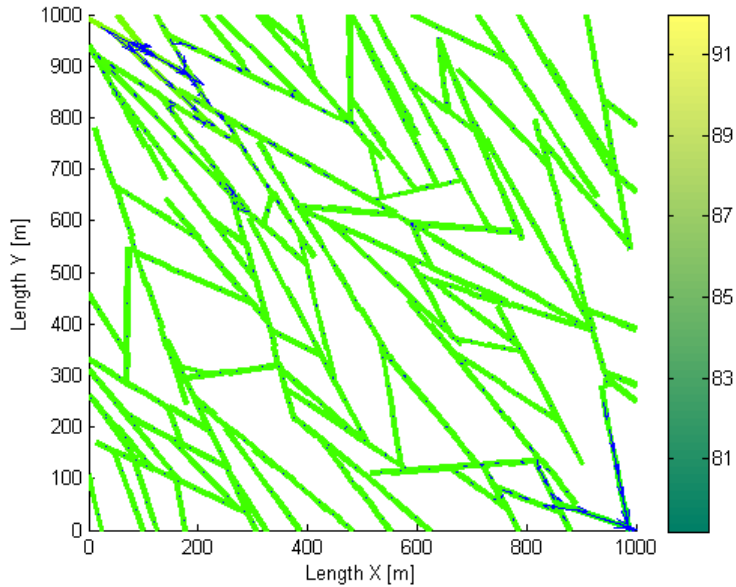


Figure 1.12: The flow and pressure in the fracture network with steam at the production zone. Injection is in the top left corner and production is from the bottom right. The pressure is given by the color of the fractures. The relative flow rate is given by the blue arrows. The largest flow rate, 10.5 kg/s, is in the bottom right corner.

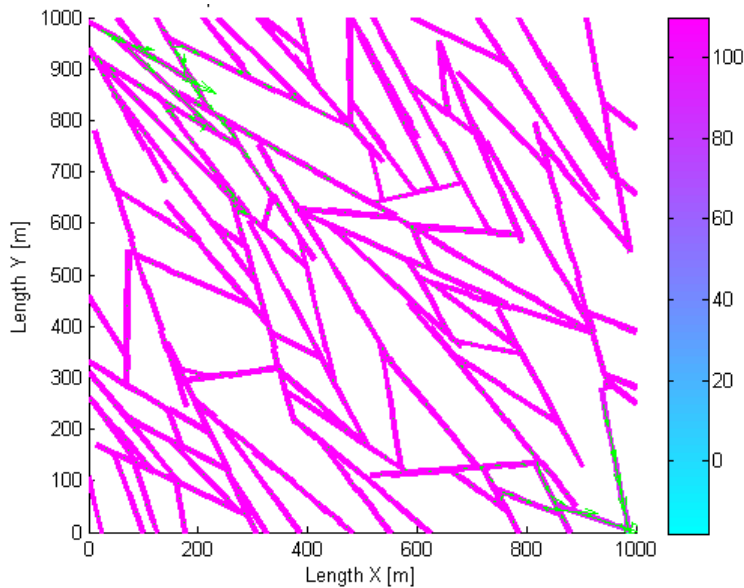


Figure 1.13: Liquid saturation and heat transfer rate in the fracture network with steam at the production zone. Injection is in the top left corner and production is from the bottom right. Liquid saturation is given by the color of the fractures. The relative heat transfer rate is given by the green arrows. The largest rate, 14.9 MW, is in the bottom right corner.

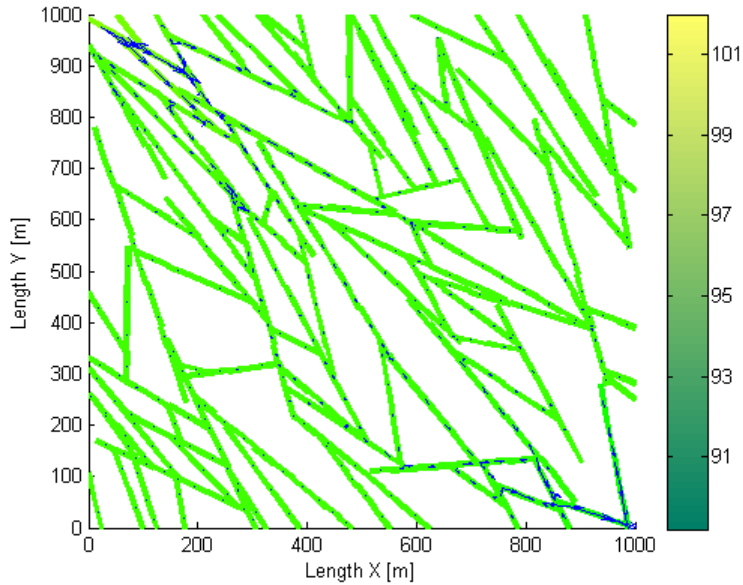


Figure 1.14: Flow and pressure in the fracture network with liquid at the production zone. Injection is in the top left corner and production is from the bottom right. The pressure is given by the color of the fractures. The relative flow rate is given by the blue arrows. The largest flow rate, 10.5 kg/s, is in the bottom right corner.

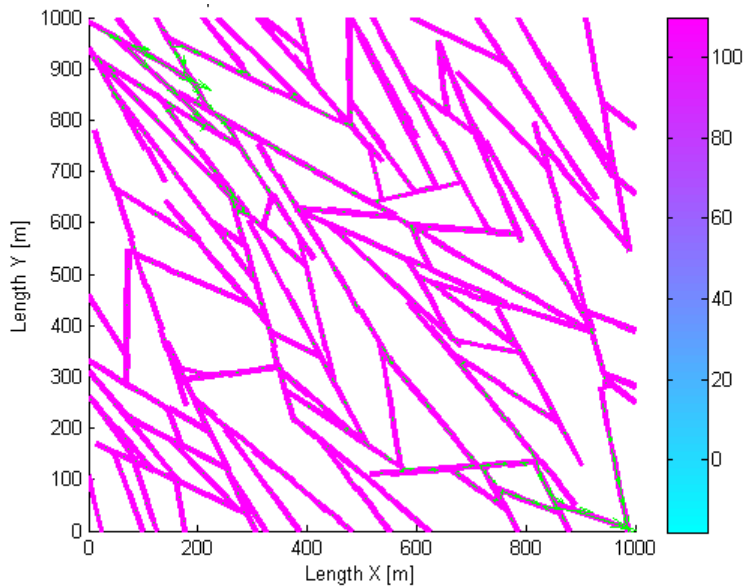


Figure 1.15: Liquid saturation and heat transfer rate in the fracture network with liquid at the production zone. Injection is in the top left corner and production is from the bottom right. Liquid saturation is given by the color of the fractures. The relative heat transfer rate is given by the green arrows. The largest rate, 14.9 MW, is in the bottom right corner.

An implication of what is being shown in these two examples is that by inducing phase change in the reservoir, we can increase the fracture matrix interaction, which in turn

increases the efficiency of heat mining from the reservoir. To be able to do this we must lower the reservoir pressure below the boiling point. In some cases, especially with EGS this might cause a reduction in the fracture aperture (i.e. permeability) surrounding the well, which in turn reduces the output flow rate. Hence, a balance between the two effects must be found.

A second observation of interest is that since the flow disperses to a great extent on its way between the injector and producer, it would not be possible to infer much about individual fractures from flow rate histories, at least not for fracture networks such as the one used in this example. It might however be possible to use the production history to infer something more broadly defined for the network, e.g. indicative parameters for fracture density, orientation or length. An investigation of this aspect is part of the direction of future research.

1.4 FUTURE WORK

Following is a summary of a number of our future goals.

The input and output routines for running discrete fracture network simulations must be improved and some exercise will be required to get comfortable with running those types of simulations. These simulations will then be used to generate a variety of production histories, and their character will be examined.

After examining the character of the discrete fracture production histories an attempt will be made to model the transformation from injector to producer. This will most likely involve inversion methods utilizing nonparametric regression models. This procedure will hopefully reveal some characteristic information of the fracture network.

Another approach to using the production history to learn about the fracture network would be to generate a large ensemble of production/injection curves for various fracture networks. This data could then be used to train an artificial intelligence algorithm (e.g. artificial neural network) to recognize the general character of the fracture network.

Finally, we are on the outlook for a viable data set for testing our work. Ideally, this data set would be densely and carefully sampled. For example, to test the Direct Correlation and ACE algorithms we need the concentration of chemicals in the reinjected brine into several wells and at least one production well, all sampled more regularly than the minimum travel time of tracer from injector to producer. Actual tracer test data would also have to be available as reference.

1.5 CONCLUSIONS

Research on characterizing fracture networks through investigation of production and injection histories has been focused on two main topics.

The first involved solving the problem of finding the travel time of tracer between multiple injectors and a single producer. The data used were synthetic tracer return curves generated

from a one dimensional analytical model. Two methods were applied to solve the problem, the ACE method and the Direct Correlation method. While neither method fully solved the problem, the Direct Correlation method did a surprisingly good job, despite its simplicity.

In order to gain a better understanding of the nature of flow through fractured media, the flow simulator TOUGH2 has been reconfigured to work with discrete fractures. Some preliminary runs were made, illustrating the effects of phase change surrounding the production zone of a fractured reservoir.

Future work will include generating production and injection histories from the discrete fracture flow simulator and using that data to do investigate the characteristics of fracture networks of various types. We have been leaning towards nonparametric methods for recovering fracture network characteristics, although, other methods are still being considered.

2. FRACTURE CHARACTERIZATION OF ENHANCED GEOTHERMAL SYSTEMS USING NANOPARTICLES

This research project is being conducted by PhD student Mohammed Alaskar, Senior Research Engineer Kewen Li and Professor Roland Horne. The main objective of this study is to investigate the possibility of using nanotechnology to characterize the fracture system (direction, shape and size of fractures) in Enhanced Geothermal Systems (EGS).

2.1 SUMMARY

The design of the nanoparticle injection experimental apparatus was completed. The nanofluid selected for initial testing was silicon oxide (SiO_2) with a narrow band of size distribution (30-100 nanometer) in water ethanol solution. The injection and sampling strategies have also been determined.

Prior to the nanoparticle injection experiment, the gas and liquid permeabilities of the core sample were measured. It was found that the liquid permeability measurement was not accurate and varied with flow rates. This may be attributed to the fact that the sandstone core sample was not saturated with water completely. Therefore, it has been decided to repeat the permeability measurements using a different Berea sandstone.

An overview of the project, requirements for nanoparticles, details of the gas and liquid permeability measurements, and the initial nanofluid injection procedure are described in this report.

2.2 INTRODUCTION

Geothermal applications require materials that are suitable for harsh environments of high pressures and temperatures. Extraordinary properties of materials made at nanoscale can provide these requirements. Therefore, it is proposed to explore the possibility of utilizing nanoparticles as sensors to characterize fracture systems. The main idea is based on the fact that certain types of nanosensors have the ability to record data such as pressure and temperature within the reservoir. Actually, temperature-sensitive nanomaterials have been already used in biomedical industry for drug delivery to particular types of body cell. For geothermal field applications, it is envisioned that the nanoparticles of different sizes and shapes can accompany the injected fluids at one well and recovered from another within the same reservoir. The nanoparticles that made their way to the producing well will be analyzed and correlated with the fracture properties.

2.3 REQUIREMENTS FOR NANOPARTICLES

Nanoparticles used in this study and ultimately in the reservoir need to be safe to handle and environmentally friendly. The particles should also be stable in suspension and disperse in solution. Moreover, the interaction affinity of such particles to the reservoir formation should be verified and the particles must not interact with rock matrix (Kanj, Funk and Al-Afaleg, 2007).

2.3.1 Selection of Nanoparticles

Monodisperse silica particles (silicon oxide, SiO_2) satisfy all essential requirements and therefore have been selected for initial experimentations with nanofluid injection. SiO_2 can remain in suspension at different concentrations and particle sizes, and have a narrow band of sizes in solution.

The conditions for the preparation of monodisperse silica particles follow the study done by Bogush, Tracy and Zukoski (1988). The nanoparticles preparation is accomplished by the hydrolysis of tetraethyl orthosilicate (TEOS) in aqueous ethanol solutions containing ammonia. Initially, particle sizes in the range of 30 – 100 nanometers are targeted.

The correlation resulting from Bogush et al., (1988) is used as an engineering tool in the determination of single-sized particles. The expression is fitted to the experimental observations and written as:

$$d = A[H_2O]^2 \exp(-B[H_2O]^{1/2}) \quad (2.1)$$

with

$$A = [TEOS]^{1/2} (82 - 151[NH_3] + 1200[NH_3]^2 - 366[NH_3]^3) \quad (2.2)$$

and

$$B = 1.05 + 0.523[NH_3] - 0.128[NH_3]^2 \quad (2.3)$$

where d is the average diameter in nanometers and the concentrations of the reagents are in the units of mol/l (Bogush et al., 1988). Figure 2.1 shows the relationship between the particle diameter obtained from the correlation and the diameters obtained experimentally. Most of the data fall within the 20% deviation lines.

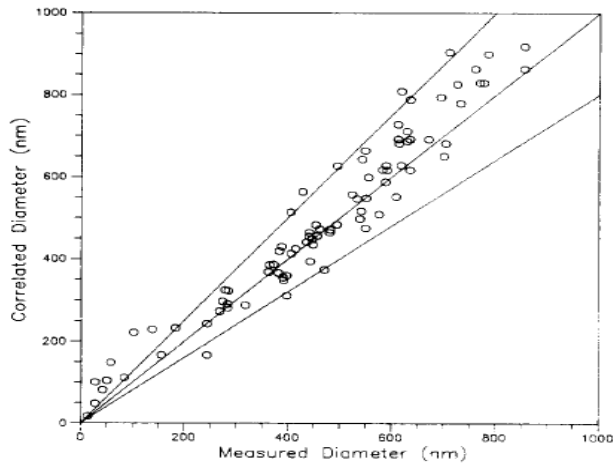


Fig. 2.1: Relationship between model and experimental diameters (from Bogush, Tracy and Zukoski, 1988).

The approach is to vary the concentration of water and ammonia while keeping the TEOS concentration constant. The dependence of the particle diameter calculated from the correlation between water and ammonia concentrations for a constant TEOS concentration of 0.17 mol/l is depicted in Figure 2.2.

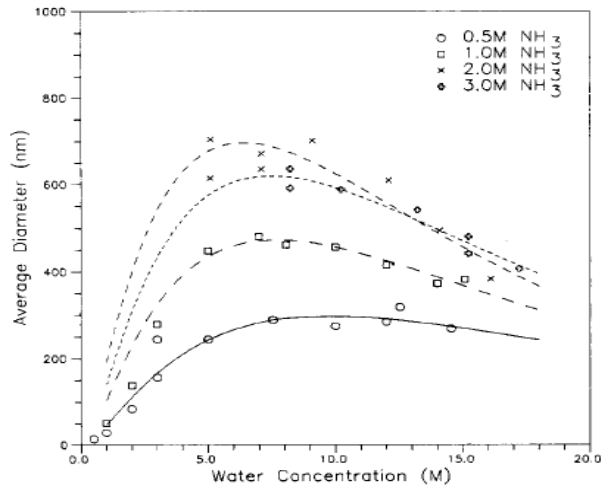


Fig. 2.2: Average particle size as a function of water and ammonia concentrations with fixed TEOS concentration of 0.17 M (from Bogush, Tracy and Zukoski, 1988).

2.3.2 Determination of Concentration and Characterization of Nanoparticles

In general, the quantity of the nanotracer produced at the sampling or exit point should be sufficient to be recognizable. As mentioned earlier, the nanofluid that will be used in our initial experiments is silicon oxide (SiO₂). The core sample is sandstone, which is also made of similar material (silica). However, there should be no concern that some of the core sample silica particles are produced as they can easily be distinguished from the nanoparticles because of the size and shape differences.

The produced nanotracer should also be at concentrations above the lower detection limit of the device used to analyze the effluent by at least factor of three. The device to be used is a Scanning Electron Microscope, SEM. The SEM can detect even one nanoparticle, even those with sizes smaller than the ones used in our experiments.

Characterization of the rock as well as the nanofluid prior to and after injection is essential. Studying the nanoparticles morphology inside the sample is of equal importance. The objective is to understand the particle size distribution and how they arrange themselves within the porous medium (Kanj et al., 2007). To this end, SEM analysis will be performed at different sections of the core sample (i.e. at the inlet, outlet and in the middle.)

2.3.3 Methodology of Injecting Nanoparticles

The nanofluid injection plan is similar to the coreflooding process suggested by Kanj et al. (2007). Figure 2.3 presents the testing plan, which involves the injection of a pore volume of nanofluid followed by a continuous injection of pure water. The pore volume will be determined by weight comparison prior to and after the full saturation of the sample. The main purpose of this process is to assess the particle size, concentration in solution and affinity to the formation rock. In this regard, at least two pore volumes plus the dead

volume (the volume of the tubes and fittings) need to be injected. The dead volume will fill the tubes completely prior to nanofluid entering the core. Following that is the first pore volume which should fill the pore spaces. The second pore volume is used to confirm the filling. The volume calculations are straightforward:

$$V_p = \pi r^2 l \phi \quad (2.4)$$

$$V_d = \pi r_t^2 l_t \quad (2.5)$$

$$V_{inj} = V_p + V_d \quad (2.6)$$

where r_t is the tube radius, l_t is the tube length, ϕ is the porosity. V_p , V_d and V_{inj} are the pore, dead and total injected volumes respectively.

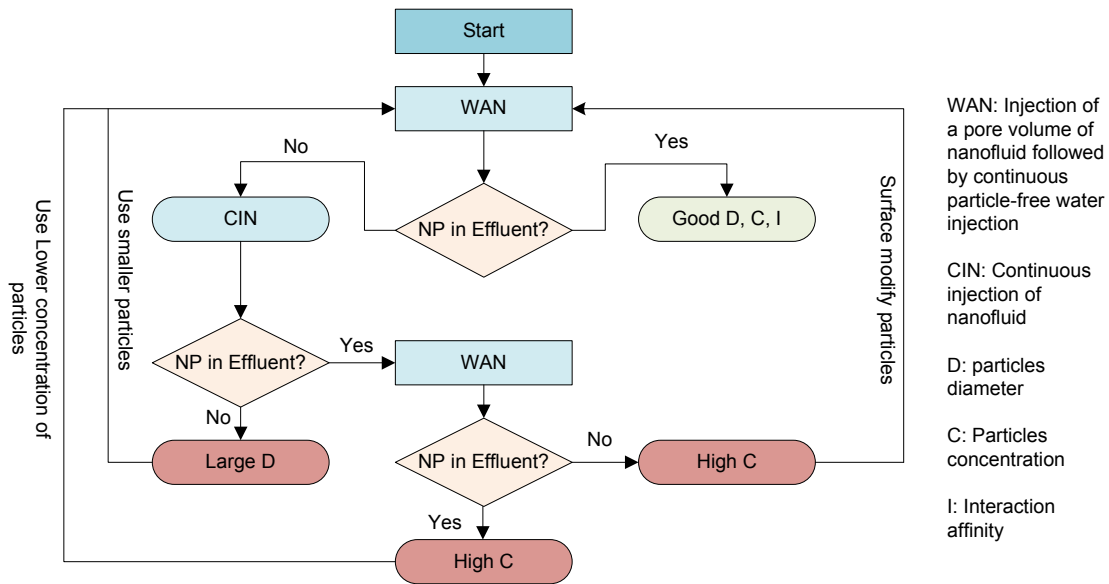


Fig. 2.3: Nanofluid testing plan (reproduced from Kanj, Funk and Al-Afaleg, 2007).

2.4 EXPERIMENTS

This section provides the details of the first attempt to inject the nanofluid (SiO_2) into a core sample. Prior to nanofluid injection, permeability measurement have been conducted to confirm the sample permeability. The core sample is sandstone of 3.8 cm in diameter and 5 cm in length.

2.4.1 Permeability Measurement

First, the gas permeability was measured. The Klinkenberg effect (gas slippage) was considered to evaluate the equivalent liquid permeability. Secondly, the liquid permeability for the same sample was also measured.

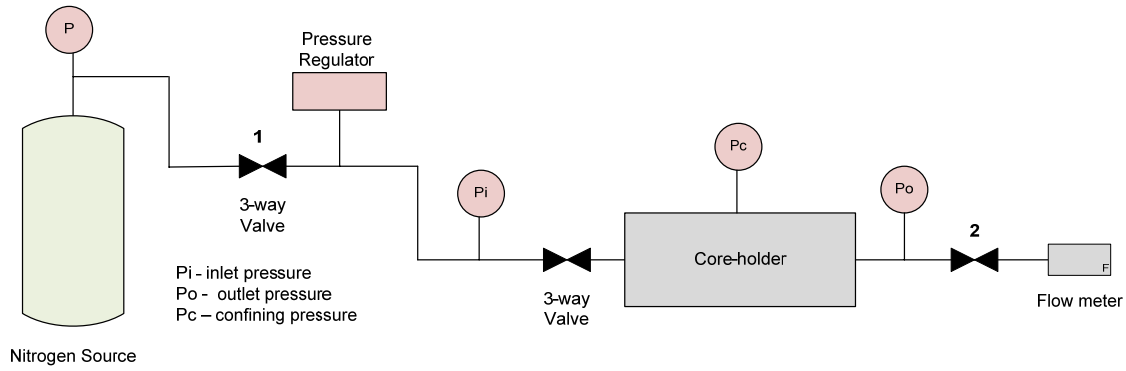


Fig. 2.4: Schematic of the apparatus for measuring gas permeability.

Figure 2.4 is a schematic of the apparatus used in the measurement of gas permeability. The pressures at the upstream (inlet) and downstream (outlet) of the core have been measured using differential pressure transducers manufactured by Celesco Company. These transducers (Model DP30) have a linearity of 0.5% and a repeatability of 0.5% full scale. The diaphragms used in the inlet transducer and outlet transducers have the range from 0 to 100 psi and 0 to 25 psi, respectively. Both differential pressure transducers were calibrated using a standard pressure gauge with an accuracy of 0.1 psi. The pressure transducer calibration curves are depicted in Figures 2.5 and 2.6. The pressure calibration curves indicate a good agreement between the standard pressure gauge and the differential pressure transducers.

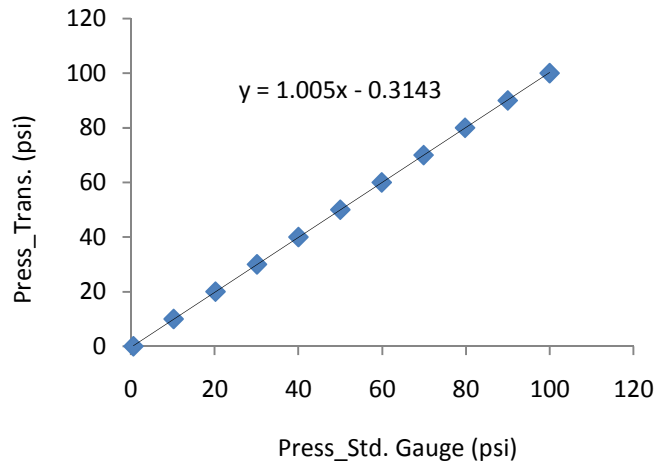


Fig. 2.5: Calibration curve of the inlet pressure transducer.

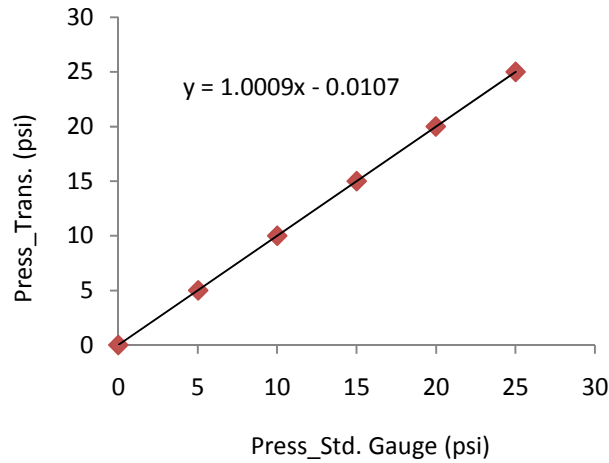


Fig. 2.6: Calibration curve of the outlet pressure transducer.

The flow rate of Nitrogen gas was measured using a mass flow meter manufactured by Matheson (Model 8272-0423). The meter has the capability to measure flow rates from 0 to 2000 cm³/minute. At low gas flow rates (from 0 to 200 cm³/minute), another mass flow transducer (Model 8172-0422) manufactured by the same company was used. The mass flow meters were calibrated using a stop-watch and graduated cylinder (as the standard method of measuring the flow rate). The calibration curves for these flow meters at room temperature are shown in Figures 2.7 and 2.8.

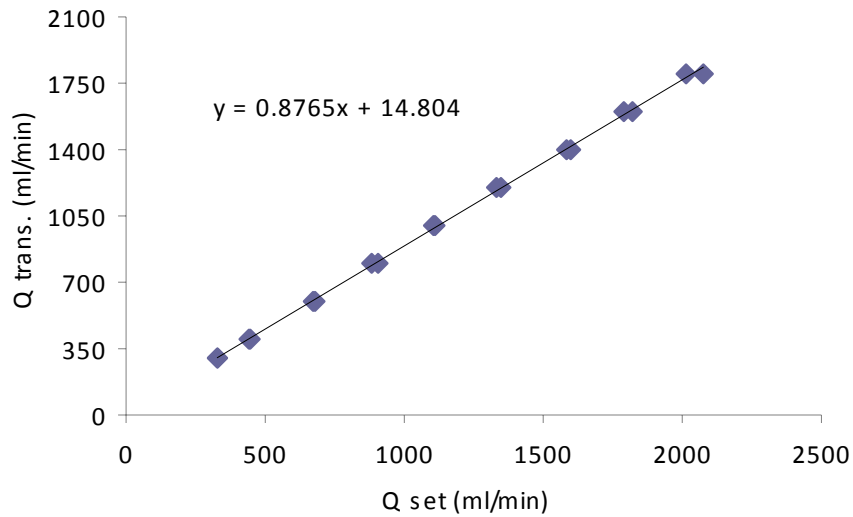


Fig. 2.7: Calibration curve of the high (2000 cm³/minute) flow rate transducer.

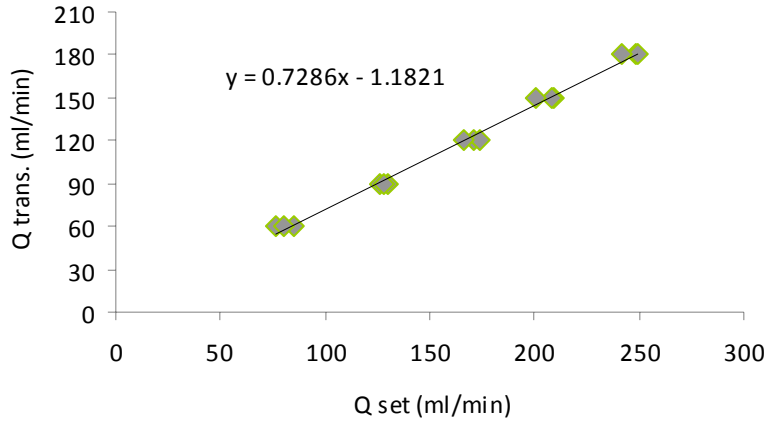


Fig. 2.8: Calibration curve of the low (200 cm³/minute) flow rate transducer.

The core was first dried in a furnace at 110°C under vacuum for 24 hours. After weighing the core sample, the core was placed inside the core-holder under a confining pressure of 500 psi. The gas permeability measurement was then started by introducing nitrogen at different flow rates and inlet pressures. The average gas permeability was found to be around 336 md by applying Darcy's law for compressible fluids which is given by:

$$k_{gas} = \frac{2\mu p_{out} q_{out} L}{A(p_{in}^2 - p_{out}^2)} \quad (2.7)$$

where μ is the viscosity (cp), q_{out} is volumetric flow rate (cm³/minute), A is the core cross-sectional area (cm²), L is the core length (cm) and p_{in} and p_{out} are inlet and outlet absolute pressures (atm).

The gas permeability as a function of the reciprocal of mean pressure is depicted in Figure 2.9. According to the Klinkenberg effect, extrapolating the straight line to infinite mean pressure (or zero reciprocal of mean pressure) intercepts the permeability axis at a point designated as the equivalent liquid permeability (Amyx, Bass, and Whiting, 1960). In Figure 2.9, the average equivalent liquid permeability is 265 md.

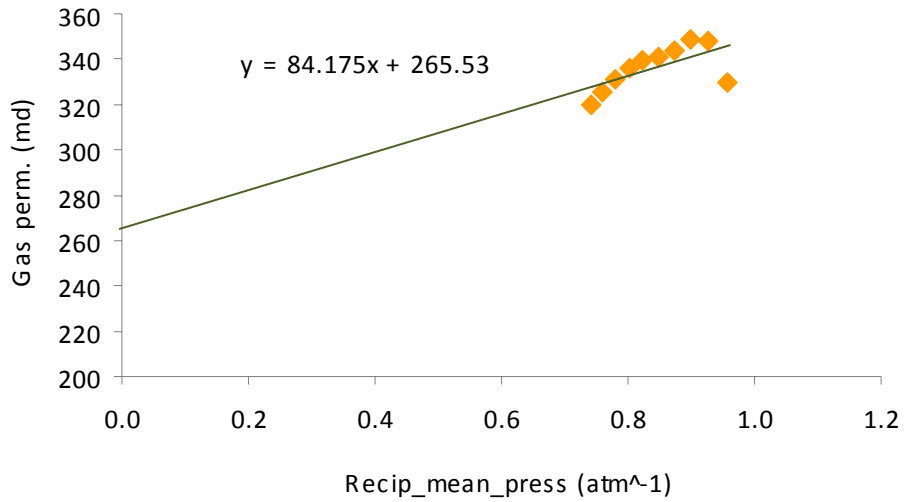


Fig. 2.9: Gas permeability versus the reciprocal of mean pressure

The liquid permeability is performed on the same core sample. Schematic of the apparatus used in the measurement of liquid permeability is shown in Figure 2.10.

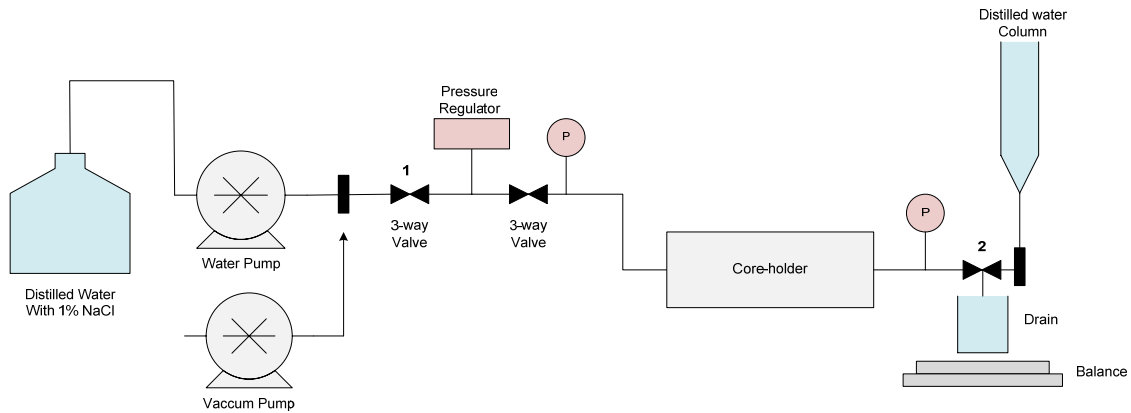


Fig. 2.10: Schematic of apparatus for liquid permeability measurement

The core sample and the related system were evacuated using a Welch Vacuum Pump (Model No. 8915A) for 4 hours at a vacuum pressure of about 100 millitorr to remove moisture. All differential pressure transducers had been calibrated previously as part of the gas permeability measurement. In addition, a water pump (Dynamax, Model SD-200) manufactured by RAININ Instrument Company was used to inject 1% NaCl brine. The minimum pumping rate of the pump is 0.05 ml/min with an accuracy of 0.01 ml/min. This pump is an automated constant-rate pump. The flow rates of the water pump were calibrated before the experiment using a stop-watch and a Mettler balance (Model PE 300).

The accuracy of the balance is 0.01g and the range is from 0 to 300 g. The calibration curve for this pump at room temperature is shown in Figure 2.11. The measured flow rates were consistent with those specified on the pump.

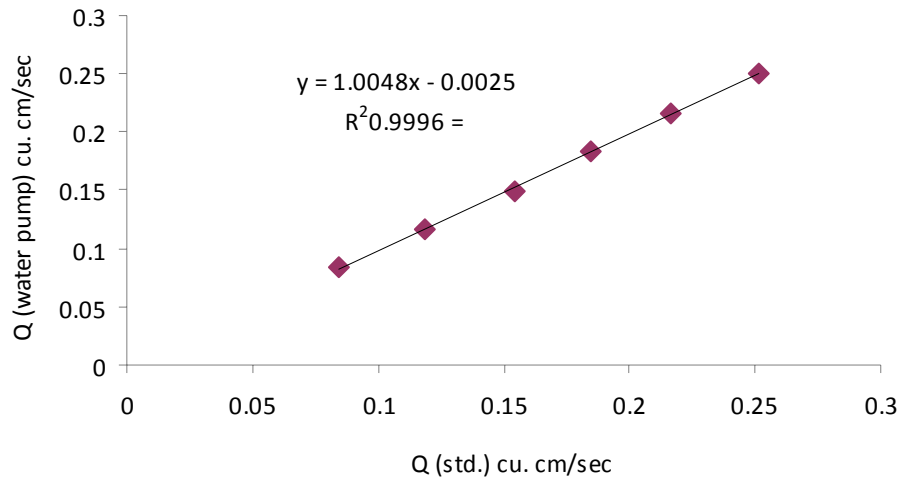


Fig. 2.11: Water pump calibration curve.

Following the evacuation, distilled water was injected for approximately 20 hours to fully saturate the core sample. The liquid permeability was then measured by introducing 1% NaCl brine using the water pump. Several flow rates were used to calculate the liquid permeability, ranging from 5 ml/min to 15 ml/min at different differential pressures. Darcy's law for horizontal flow is utilized to compute the permeability. Darcy's law for horizontal flow is given by:

$$k_{liq} = \frac{q\mu L}{A\Delta p} \quad (2.8)$$

where q is the volumetric flow rate (ml/sec), μ is the viscosity (cp), L the core length (cm), A the cross-sectional area (cm²) and Δp the differential pressure across the core sample (atm).

The average liquid permeability was found to be around 150 md. Various estimated permeability values are plotted against the flow rate in Figure 2.12. A fluctuation of about 15 md was observed in the permeability measurements as we increased the flow rate.

The core remained saturated while preparing the experiment for the nanofluid injection. Prior to the nanofluid injection, the permeability was remeasured, however was found to differ by almost 40% from that previously determined. We speculate that this may be attributed to different possibilities:

1. Swelling of clay in the core: the core sample is sandstone which contains clays. It is known that clays do swell when exposed to distilled water.
2. Air in the pore spaces: it is possible that some air was trapped and not removed by evacuation.

To eliminate the possibility of swelling, it has been decided to repeat the permeability measurements using a different core sample. The new core sample is Berea sandstone of 3.8 cm in diameter and 6 cm in length. A careful evacuation will also get rid of air trapped inside the porous medium.

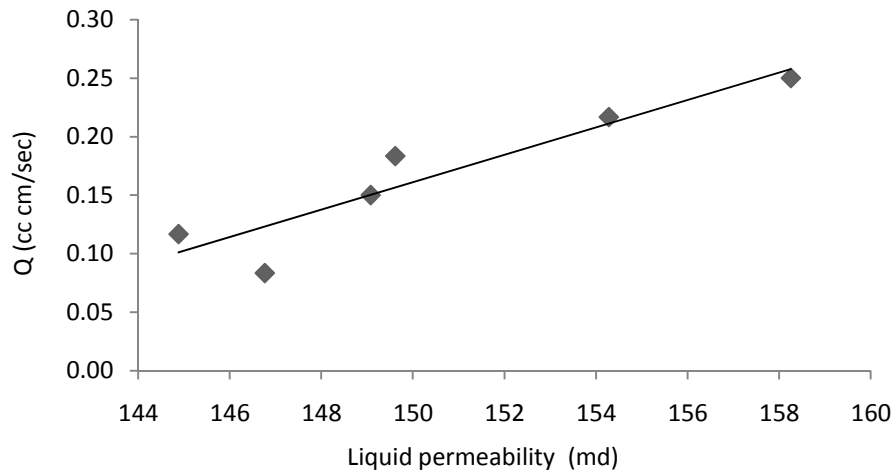


Fig. 2.12: Liquid permeability measured at different flow rates.

2.4.2 Nanofluid injection experiment

To explore the possibility of using the nanoparticles to characterize the fractures, an experimental investigation has been started to assess the suitable particle size and verify their transport through the formation rock. The coreflood apparatus was used to imitate the reservoir conditions. A schematic of the apparatus that will be used in the nanofluid injection experiment is shown in Figure 2.13. Nanofluid solution is contained in a pressure vessel downstream of the water pump. The nanofluid will be injected to the core with the aid of nitrogen pressure. The configuration also allows for injection of particle-free water, without interrupting the flow.

Initially, the experiment will not consider the temperature effect, so will be conducted at room temperature. The nanofluid prepared contains silicon oxide (SiO₂) particles of sizes between 30 and 100 nanometers. It is of interest to inject the nanoparticles with a narrow band variation in sizes and determine which sizes come out in the effluent.

The concentration of the nanofluid should be considered to ensure suspension of the particles in the solution. Following the general procedure outlined earlier, two pore

volumes plus dead volume of the nanofluid will be injected followed by a continuous injection of pure water. The effluent will be collected and analyzed. Slices at both the inlet and outlet of the core sample will be cut and analyzed using Scanning Electron Microscope (SEM). The purpose of this analysis is to evaluate the particle distribution inside the sample and to have a better idea of how these particles arrange themselves within the pore network.

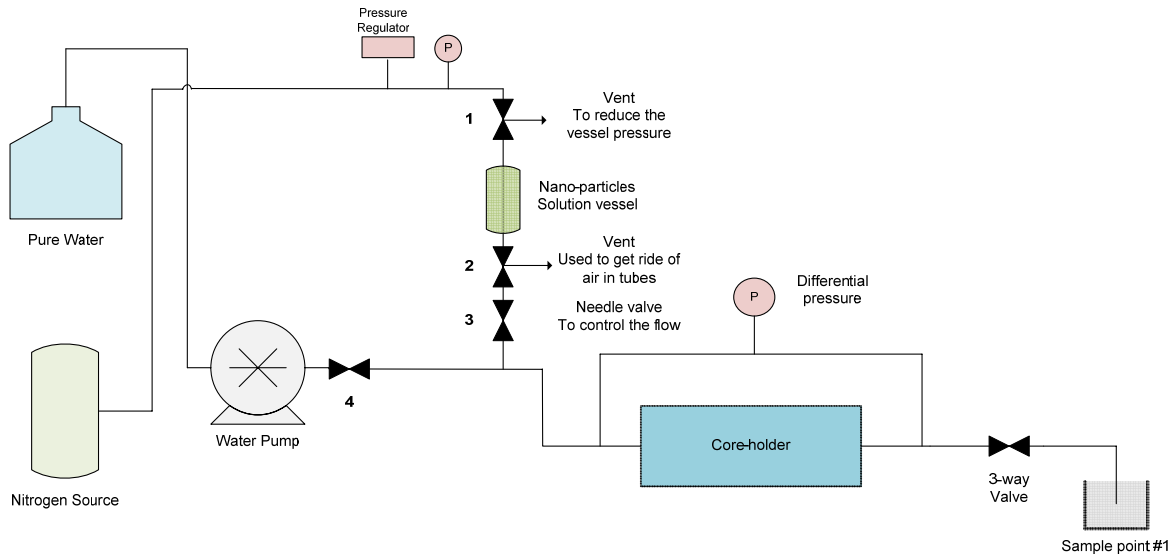


Fig. 2.13: Experimental apparatus for nanofluid injection.

A good analysis of the samples requires good sampling strategy. The following provides the broader aspects of the nanofluid injection sampling procedure.

The arrival time for injected nanofluid is the time at which the maximum concentration is reached at the exit point. This is determined by sampling before and after the peak. Sampling immediately following the injection should be very frequent. As time progresses, the sampling frequency can be lowered. There is no harm in taking samples more frequently than necessary as long as time required to collect the samples is not an issue. Not all these samples need to be analyzed. The infrequent samples could indicate the trend of the returning tracer and more details (if needed) can be obtained by analyzing the samples in between. If the samples have not been taken frequently enough, there is no way to recover the results without repeating the experiment. Figure 2.14 is an example of recovery curve of a radioactive tracer injected in a geothermal field tracer test.

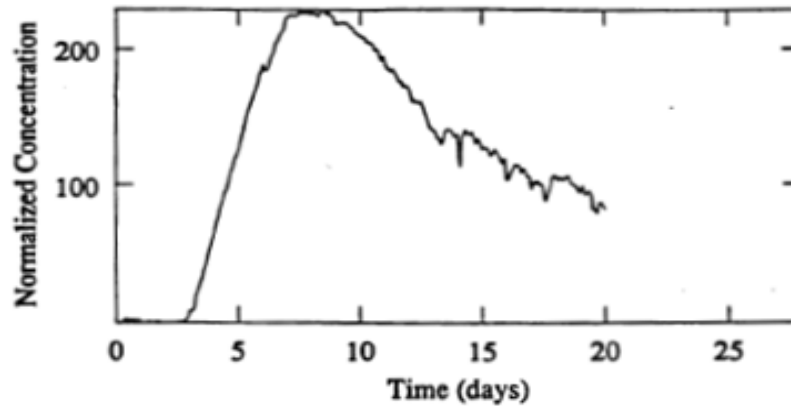


Fig. 2.14: Radioactive tracer recovery at Wairakei well WK116 from injection into WK80 (data from McCabe, Barry and Manning, 1983).

To be specific, the way the nanofluid sampling is envisioned is as follows:

- Total time for the experiment is two hours;
- Initially, injection of nanofluid will be performed. The first sample should collect the effluent resulting from the nanofluid injection only (at time $t = 0$);
- Following the nanofluid injection will be a continuous injection of distilled water for two hours at the rate of 0.5 ml/min;
- A sample will be collected every 4 minutes, making about 30 samples in total;
- One third of the total samples plus the sample resulting from the nanofluid injection will be analyzed;
- In case more details are required, the samples in between will be examined. This should optimize the analysis time.

2.5 FUTURE WORK

We will shortly start the injection of the nanofluid and perform the analyses of the effluent samples and slices of the core. After that, nanofluids with different specifications (particle size and concentration) will be injected and results will be compared. It is also planned to repeat these experiments on fractured rock samples. Temperature effect will then be studied by conducting the experiment at elevated temperature to mimic the reservoir temperature.

3. REFERENCES

- Amyx, J. W., Bass, D. M. Jr., and Whiting, R. L. (1960), *Petroleum Reservoir Engineering, Physical Properties*. McGraw-Hill Book Co.
- Bogush, G. H., Tracy, M. A., and Zukoski, C. F., IV., "Preparation of Monodisperse Silica Particles: Control of Size and Mass Fraction," *Non-Cryst. Solids* **104** (1988) 95.
- Breiman L. and Friedman J.H.: "Estimating Optimal Transformations for Multiple Regression and Correlation," *Journal of American Statistical Association*, 80, (September 1985), 580-619.
- Fienen, M.N., Luo, J. and Kitanidis, P.K., "A Bayesian geostatistical transfer function approach to tracer test analysis," *Water Resources Research*, 42, W07426, 2006.
- Horne, R.N., and Szucs, P., "Inferring Well-to-Well Connectivity Using Nonparametric Regression on Well Histories," *Proceedings, Thirty-Second Workshop on Geothermal Reservoir Engineering*, Stanford University, Stanford, California, January 22-24, 2007.
- Kanj, M., Funk, J. and Al-Afaleg, N., "Towards In-situ Reservoir Nano-Agents," Saudi Aramco, Dhahran, Saudi Arabia, 2007.
- Karimi-Fard, M., Durlafsky, L.J. and Aziz, K., "An efficient discrete fracture model applicable for general purpose reservoir simulators," SPE 79699, presented at the SPE Reservoir Simulation Symposium held in Houston, TX, 3-5 February 2003.
- McCabe, W. J., Barry, B. J., and Manning, M. R., "Radioactive Tracers in Geothermal Underground Water Flow Studies," *Geothermics*, Vol. **12**, 83-110, 1983.
- McClure, M., "Linking TOUGH2 to DFN code by M. Karimi-Fard" personal communication, 2008.
- Nomura, M. and Horne, R.N., "Data processing and interpretation of well test data as a nonparametric regression problem," SPE 120511, presented at the SPE Western Regional Meeting held in San Jose, CA, 24-26 March 2009.
- Shewchuk J.R., "Triangle: Engineering a 2D Quality Mesh Generator and Delaunay Triangulator," *Applied Computational Geometry: Towards Geometric Engineering*, Volume 1148 of Lecture Notes in Computer Science, pages 203-222, Springer-Verlag, Berlin, May 1996.